

## Two new kinds of nanodiamonds with the structure of controlled $sp^3/sp^2$ carbon ratio and carbon atom dimer by the cleavage plane mechanical stripping crush separation preparation technology

Liuxi Guo, Jinzhong Yang, Yongqi Liu, Jingru Shao, Yanqiang Wu & Shuxi Dai

To cite this article: Liuxi Guo, Jinzhong Yang, Yongqi Liu, Jingru Shao, Yanqiang Wu & Shuxi Dai (2018) Two new kinds of nanodiamonds with the structure of controlled  $sp^3/sp^2$  carbon ratio and carbon atom dimer by the cleavage plane mechanical stripping crush separation preparation technology, Fullerenes, Nanotubes and Carbon Nanostructures, 26:1, 42-51, DOI: [10.1080/1536383X.2017.1402005](https://doi.org/10.1080/1536383X.2017.1402005)

To link to this article: <https://doi.org/10.1080/1536383X.2017.1402005>



Published online: 04 Jan 2018.



Submit your article to this journal [↗](#)



View related articles [↗](#)



View Crossmark data [↗](#)



# Two new kinds of nanodiamonds with the structure of controlled $sp^3/sp^2$ carbon ratio and carbon atom dimer by the cleavage plane mechanical stripping crush separation preparation technology

Liuxi Guo<sup>a</sup>, Jinzhong Yang<sup>a</sup>, Yongqi Liu<sup>a</sup>, Jingru Shao<sup>a</sup>, Yanqiang Wu<sup>b</sup>, and Shuxi Dai<sup>c</sup>

<sup>a</sup>Zhengzhou Sino-Crystal Diamond Joint-stock Co. Ltd, Zhengzhou, Henan Province, PR China; <sup>b</sup>Henan Yuxing Sino Crystal Micron Diamond Co. Ltd, Zhengzhou, Henan Province, PR China; <sup>c</sup>Institute of Microsystem, School of Physics and Electronics, Henan University, Kaifeng, Henan Province, PR China

## ABSTRACT

Two new diamond nanostructures of nanoparticles and multilayer nanosheets were prepared through cleavage plane crush separation preparation technology by synthetic diamond as starting material. All samples were characterized by X-ray diffraction (XRD), transmission electron microscopy (TEM), scanning electron microscopy (SEM), Raman spectroscopy (Raman), and  $^{13}\text{C}$  Solid-state Magic Angle Spinning Nuclear Magnetic Resonance (MASNMR). The influence of precipitation time on the particle size, crystalline, morphology, structure of the nanostructures was investigated. The crystalline phase of the final products was determined as diamond phase. More importantly, the morphology of nanodiamond was closely related to the structure. Nanoparticles consisted of carbon atom dimer structure on the surface, while the multilayer nanosheets contained unsaturated  $sp^2$  hybridization carbon, and the unsaturated  $sp^2$  hybridization carbon contents increased with increasing particle size. Possible formation mechanisms of diamond nanostructures with various structures and morphologies were proposed in detail.

## ARTICLE HISTORY

Received 7 September 2017  
Accepted 3 November 2017

## KEYWORDS

Nanodiamond; nanoparticles;  
Multilayer nanosheets;  
Unsaturated  $sp^2$   
hybridization carbon

## 1. Introduction

In the past two decades, carbon-based nanomaterials including fullerenes, carbon nanotubes (CNTs), graphene (GN) have triggered a new wave of experimental and theoretical studies due to their unique structures, extraordinary physical and chemical properties, and various potential applications.<sup>[1–11]</sup> Nanodiamond (ND), as a very promising member of the carbon nanomaterials family, has received relative less attention compared to other carbon family members. Recently, the interests in nanodiamond have been quickly increasing owing to their unique physical and chemical properties such as high level of hardness, strength, and thermal conductivity, electrical resistivity and chemical inertness<sup>[12]</sup> etc. And nanodiamond (ND) has been increasingly applied in many fields including electronic, optics, mechanics, superconducting materials and biological medicines.<sup>[13–17,26]</sup> with exhibiting various superior characteristics such as optical transparency, chemical inertness, extremely high level of hardness, stiffness, and strength, etc.

It is well established that nanodiamond (ND) can be manufactured by the application of detonation of carbon-containing explosives in a steel chamber at high temperature and high pressure (HTHP,  $\sim 3,000$  K, 300 kbar) instantaneously.<sup>[18–20,23]</sup> which is a kind of dynamic high temperature and high pressure synthesis method.<sup>[19]</sup> There are also some byproducts such as nanographite and amorphous carbon in addition to nanodiamond.<sup>[21,23]</sup> The purity of final ND is only 95% – 97% after the

purification treatments with acid oxidation liquid purification method.<sup>[18]</sup> The liquid-phase purification is not an environmentally friendly process and requires expensive corrosion-resistant equipments and costly waste disposal processes and also results in additional contamination or significant losses of the diamond phase.<sup>[31]</sup>

So far, nanodiamond can be only used in an inexpensive large-scale synthesis of ND with the following three factors importantly effecting the synthesis results.<sup>[18,21]</sup> First, carbon-containing explosives as the starting materials must have the following conditions, producing enough high temperature and pressure during the explosion, producing enough active carbon atoms during the explosion and enough molecular structures with active groups. Up to now, TNT and RDX explosive mixture are generally used as raw materials. TNT explosive has been applied as carbon source and RDX explosives as the booster.<sup>[20]</sup> Second, explosive charge form and structure determined the uniformity of the reaction. And the uniformity of reaction contributed towards the formation of nanodiamond and the improvement of a production rate. The relationship between the average nanodiamond particle diameter of  $d$  and the explosive charge diameter of  $D$  had been also given as  $d \propto D^{1/3}$ .<sup>[22]</sup> Third, the protecting medium had an important influence on the yield of nanodiamond.<sup>[21,23–24]</sup> Nanodiamond rate obtained by water as protecting medium is higher than other protecting medium such as  $\text{CO}_2$ , air and  $\text{N}_2$ .

**CONTACT** Yanqiang Wu  [wlsiyang@163.com](mailto:wlsiyang@163.com)  Henan Yuxing Sino Crystal Micron Diamond Co., Ltd, Zhengzhou, Henan Province, PR China;  
Shuxi Dai  [shuxidai@henu.edu.cn](mailto:shuxidai@henu.edu.cn)  Institute of Microsystem, School of Physics and Electronics, Henan University, Kaifeng, Henan Province, PR China.

Color versions of one or more of the figures in the article can be found online at [www.tandfonline.com/lfnn](http://www.tandfonline.com/lfnn).

Furthermore, the morphology of ND obtained by explosive detonation synthesis is usually hard aggregated nanoparticles having a truncated octahedral architecture with average particle diameter of about 5 to 10 nm.<sup>[19]</sup> Due to a large number of unsatisfied surface carbon atoms and a large surface to volume ratio, ND exhibits a very high surface reactivity of a single particle compared to that of other carbon nanostructures. Thus, ND disperses in aqueous solution usually spontaneously form clusters of tens to hundreds nanometers with a lower free energy, whether the physical ultrasonic or chemical dispersion is adopted.<sup>[25–30]</sup>

The detonation synthesis of ND was first discovered in Soviet Union about 50 years ago.<sup>[32]</sup> As well as we know, nanodiamond thin films now can be easily produced either as using chemical vapor deposition (CVD) techniques.<sup>[14,33–34]</sup> However, the nanodiamond powders can only prepared by the detonation of carbon-containing explosives technique, which has not made obvious progress for long times. Here, we reported a new cleavage plane crush separation preparation technology by using synthetic diamond as starting material. This new kind of ND preparation technology demonstrates the possibility of preparation of nanodiamond without introduction of defects and it is also simple, inexpensive and environmental friendly. In this paper, two new kinds of ND powders were prepared feasibly by the new preparation technology with synthetic diamond as raw material, which is different from the detonation of carbon-containing explosives. The influence of preparation process on the particle size, crystalline, morphology, structure of the nanostructures was investigated. Possible formation mechanisms of diamond nanostructures with various structures and morphologies were proposed in detail.

## 2. Experimental

### 2.1. Materials

All chemical reagents are analytical reagent (AR). Artificial diamonds (Product model: SCD02) were purchased from Zhengzhou Sino-Crystal Diamond Joint-stock Co., Ltd. Deionized water with a minimum resistivity of 20.0 MΩ·cm, was obtained from a Millipore deionization system. Sodium silicate nonahydrate (Na<sub>2</sub>SiO<sub>3</sub>·9H<sub>2</sub>O) was bought from Tianjin Hengxing chemical preparation Co., Ltd. Hydrochloric acid (HCl), sulphuric acid (H<sub>2</sub>SO<sub>4</sub>), and perchloric acid (HClO<sub>4</sub>) were obtained from Tianjin Kemiou Chemical Reagent Co., Ltd and sodium hydroxide (NaOH) was bought from Luoyang Chemical Reagent Co., Ltd.

### 2.2. Preparation of products

The preparation process is shown in Fig. 1. First, the artificial diamonds were fed into the air stream mill by feeding inlet.

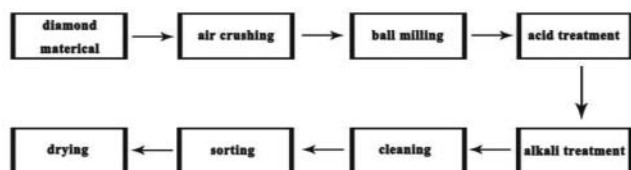


Figure 1. The diagrammatic flow sheet illustrating the preparation process.

The feeding speed is 0.45 kg/h, and the speed of the classification of impeller is 18000 r/min, and crushed gas pressure is 0.8 MPa. And then crushed products were obtained with median particle size (D50) of about 4 μm. The next step is feeding the crushed products into the ball mill. The mass ratio of the stainless steel ball and crushed products is 7:1. The diameter of the stainless steel ball is 1 mm. The rotate speed of the ball mill is 800 r/min, and the ball milling time is 4 h. After the ball milling, acids were used to remove the impurity in the products by two steps. First, the mass fraction of 10% dilute hydrochloric acid was used to remove metal and metal oxide impurities in products in the reaction vessel at room temperature. The mass ratio of hydrochloric acid to products is 1:3, and reaction time is 2 h. When the reaction is finished, the products were cleaned with deionized water until the pH value of cleaning liquid is about 7. And then the mixture acid was used to remove graphite impurities in the reaction vessel at 160°C for 1 h. The mixture acid is composed of sulphuric acid and perchloric acid which the mass fractions are 96% and 70% respectively. The mass ratio of mixture acid and products is 1:1. When the reaction is finished, the products were cleaned with deionized water until the pH value of cleaning liquid is about 7. After the acid treatment, sodium hydroxide was used to remove pyrophyllite impurities twice in the reaction vessel at 240°C for 2 h with the mass ratio of sodium hydroxide and products of 2:1, and then cleaning the products with deionized water until the pH value of cleaning liquid is about 7. Next step, sorting process covers two sorting technology, precipitating separation and centrifugal separation. Precipitating separation equipment is showed in Fig. 2, Φ220 × 300 mm. According to STOKES' law

$$v_0 = \frac{\delta - \rho}{18\eta} g d^2 \quad (1)$$

where  $\delta$  is the density of the particle,  $d$  is the particle size,  $\rho$  is the density of the liquid medium, and  $\eta$  is liquid medium viscosity. Under the condition of the same sedimentation distance, the speed of sedimentation  $v_0$  is only related to the diameter of the particle  $d$  in the same liquid medium. Therefore, according to the difference of sedimentation velocity of different size of particles, the particle size is classified. Cleaned products (330 g) were put into the sodium silicate solution with a mass concentration of 0.05%. The solution of mixed products was treated by ultrasonic wave for 30 min. After then, deionized water was added into the beaker to the upper scale line, and keep still after stir well. And 36 h later, upper liquid was extracted with the pumping pipe until under the scale line, with the distance  $h$  between upper scale line and under scale line of 150 mm. Centrifugal separated the extraction of the upper liquid. The density of the upper liquid was adjusted to between 0.9 and 1. Two-thirds of the upper liquid was taken in the centrifuge tube after each centrifugation for cyclic centrifuged three times for each 10 min with the speed of the centrifuge of 8000 r/min. And then the supernatant liquid precipitation was obtained for different times after centrifugation at room temperature, the results are shown in Table 1, and then dried in a vacuum oven for 6 h at 300°C.



Figure 2. Schematic diagram of the precipitating separation equipment.

### 2.3. Characterization

XRD patterns of the samples were collected with a Philips X'Pert Pro MPD X-ray diffraction system (XRD, Cu-K $\alpha$  radiation,  $\lambda = 0.154056$  nm) operated at 40 kV and 40 mA. All the samples were measured in the continuous scan mode in the  $2\theta$  range of 10–90°, using a scan rate of 0.02 deg/s. The crystallite size was calculated using the Scherrer equation. Scanning electron microscopic (SEM) was performed using Nova NanoSEM450, while transmission electron microscopy (TEM) observation was undertaken under JEOL JEM-2011 microscope with accelerating voltage of 200 kV and selected-area electron diffraction (SAED) was employed to characterize the samples. The Raman spectra were collected using a Renishaw RM-1000 cofocal microscopic Raman spectrometer with an air-cooled

Table 1. Table of sorting parameters of different size of products.

Particle size/nm	Precipitation separation time/h
5	360
50	228
100	192
200	180
250	168

CCD detector, the operating wavelength was 532 nm by He-Ne laser.  $^{13}\text{C}$  solid state NMR spectra were conducted on a 600 MHz Bruker spectrometer.

### 3. Results and discussion

Figure 3 presents the XRD diffraction pattern and SEM image of the starting material. The XRD pattern exhibited two primary diffraction peaks ( $2\theta = 43.7, 75.1^\circ$ ) that can be assigned to the diamond phase. The strong and narrow diffraction peaks indicated that the raw materials were well crystallized diamond structure. From Figure 3b, we can find that the raw material is complete hex-octahedron structure with a narrow particle size distribution of 100–120  $\mu\text{m}$ .

Different particle size and crystallinity of nanostructured diamond samples were obtained via cleavage plane crush separation preparation technology using synthetic diamond as raw material. Figure 4 shows the typical XRD diffraction pattern of the products with different particle size. The phase composition and purity of all the products had been identified from the XRD patterns in Fig. 4a. The peak locations and relative intensities for samples are cited from the Joint Committee on Power Diffraction Standards (JCPDS) database. The diffraction peaks located at 43.9, 75.3° are corresponding to (111) and (220) reflections of face-centered cubic (fcc) structure of diamond phase with the standard lattice constant of  $a = 3.567$  Å (JCPDS 79-1473), respectively. All the products had been confirmed to be diamond phase, the other phase had not been found. Specially, Fig. 4a inset map shows the XRD diffraction pattern of sample a, the weaker and broader diffraction peaks ( $2\theta = 43.9, 75.3^\circ$ ) than other particle size samples b-e. The results indicated that a sample were poorly crystallized diamond structure and partly amorphous.

Average crystallite sizes of all the products were estimated using Scherrer equation:  $D = 0.89\lambda / (\beta \cos\theta)$ ,<sup>[35]</sup> where  $\lambda$  is the employed X-ray wavelength,  $\theta$  is the diffraction angle of the most intense diffraction peak, and  $\beta$  is the full width at half maximum of the most intense diffraction peak (FWHM). Figure 5 shows the average grain sizes of the different particle size products with different precipitation separation time. The average grain size of the different particle size products varied between 3 nm and 30 nm with increased particle size. Moreover, it should be noted that the average size of sample a is smaller than other particle size. The average grain size of sample a is the minimum about 3.5 nm, and increased slightly with increased particle size and achieved the maximum value of about 26 nm when the particle size is 200 nm. Then the average grain size decreased and finally reached the value of about 23 nm when the particle size is 250 nm. Obviously, the average grain is related to the particle size.

Figure 6 show that as-prepared samples with increased particle size consist nanoparticles and nanosheets, which is different from nanodiamond by explosive detonation. Sample a shows carbon nanoparticles with particle size of about 5 nm, and average particle size is about 3 nm which is well consistent with XRD result, as showed in Fig. 6a. The morphology of sample b-e is multilayer carbon nanosheets. The enlarged images (Fig. 6 b1-e1) shows that the layer thickness of the carbon nanosheets is gradually thickened with increased particle size. Fig. 6 a2-e2 presents the HRTEM investigations from the

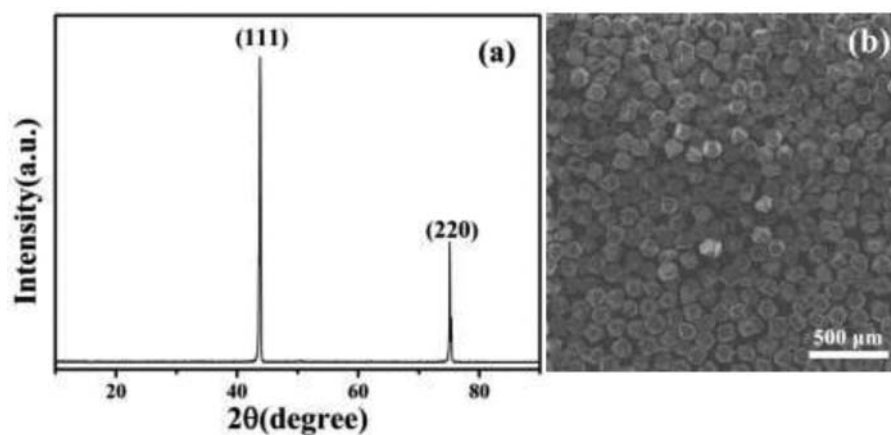


Figure 3. XRD pattern (a) and SEM (b) image of the artificial diamond starting material, respectively.

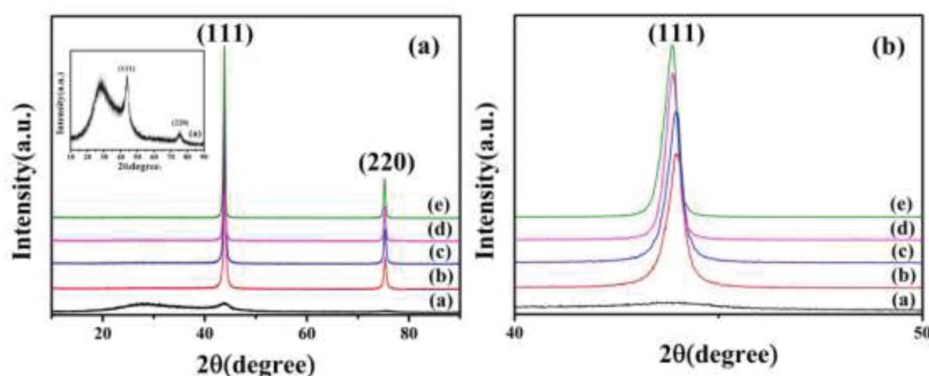


Figure 4. Wide-angle (a) and 40–50° (b) XRD patterns of the different particle size nanodiamond products. *a* 5 nm *b* 50 nm *c* 100 nm *d* 200 nm *e* 250 nm, respectively. Inset map is the XRD pattern of the 5 nm product.

carbon nanoparticles and carbon nanosheets, respectively. However, it should be noted that the existence of the amorphous carbon and lattice image showed in Fig. 6 a2, which is in agreement with XRD result. The lattice images of carbon nanoparticles and carbon nanosheets were clearly observed. From the distance between the adjacent lattice fringes, we can assign the lattice plane on the carbon nanoparticles and carbon nanosheets. The nanoparticles showed that lattice fringes of  $d = 0.21$  nm for the (111) plane of the diamond phase. The lattice images of the nanosheets were clearly observed, which

indicated that these nanosheets had high degrees of crystallinity. The distance between the lattice fringes ( $d = 0.21$  nm) in the aligned nanosheets can be assigned to the interplanar distance of the diamond phase, which is well coordinated with XRD results. Further observation by SAED (inset image in Fig. 6) confirmed that nanoparticles and nanosheets had different crystal structure, the nanoparticles had a polycrystalline diamond structure, and the nanosheets were single crystalline diamond structure.

Figure 7 presents the SEM results of the different particle size carbon nanosheets. The insets as shown in Figure 7 are the cross-sectional images of the different particle size carbon nanosheets. It is clearly shown that the change of the morphology. From Figure 7a and 7b, we can find that the diamond nanosheets array was random in size with the length distributing from 10 nm to 200 nm. Figure 7c and 7d show that diamond nanosheets are uniformly distributed with a fairly small length deviation, which varied between 200 nm and 300 nm. In addition, the layer thickness of the carbon nanosheets is gradually thickened with increased particle size, which is agreed with the TEM results.

From the above results, we supposed that the formation of diamond nanostructures with various morphologies in the present research could be thought of as a nonclassical pathway of cleavage plane stripping crush under the action of mechanical force. The relevant formation mechanism of the nanocrystalline diamond with different morphologies can be described

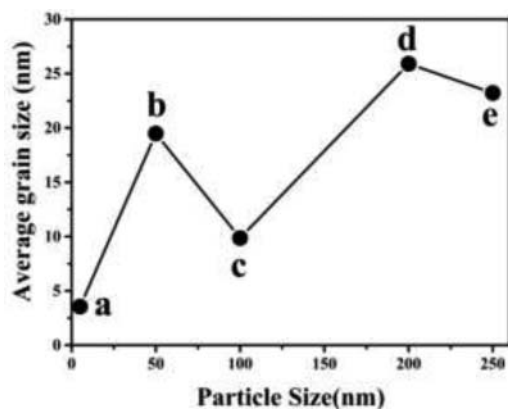
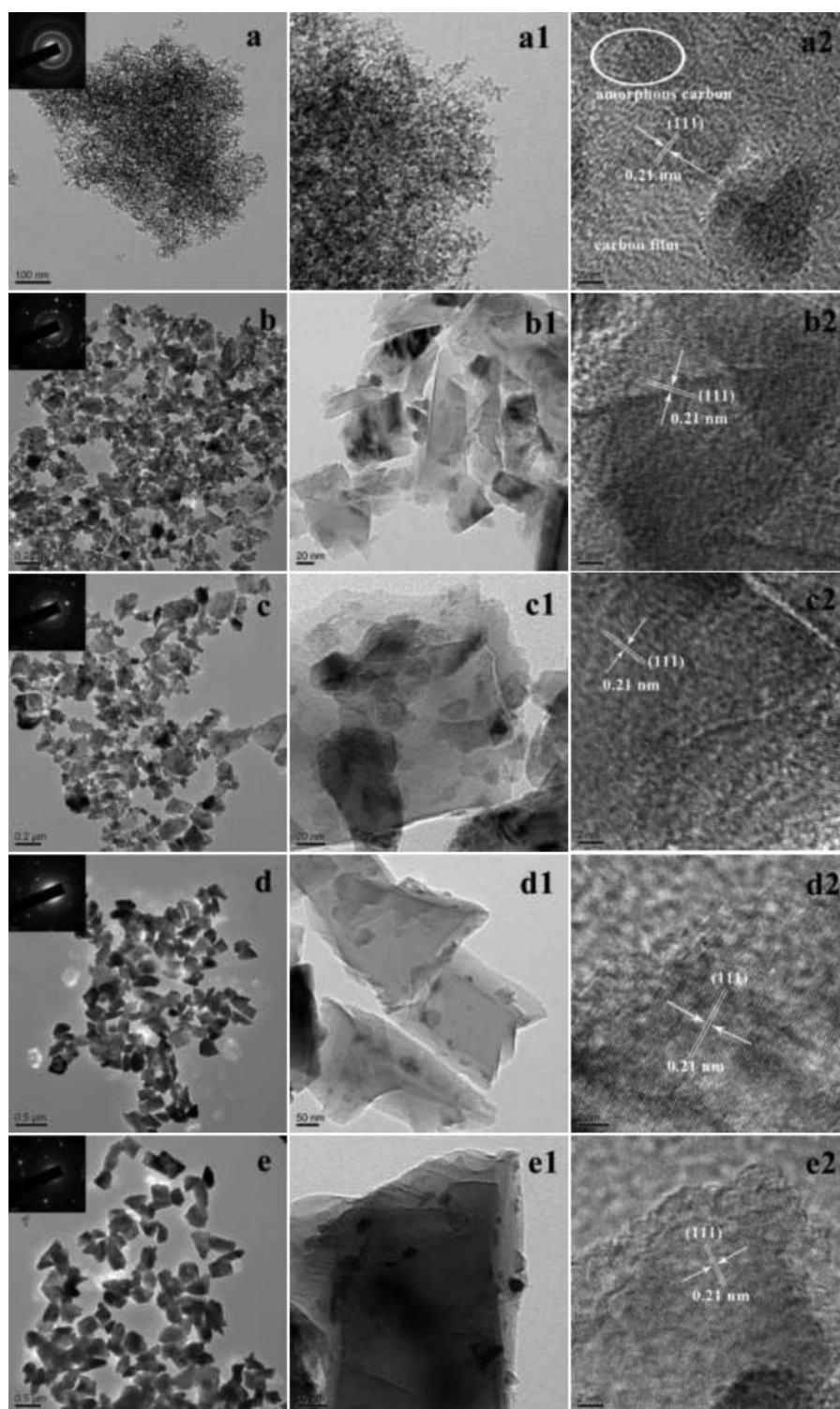


Figure 5. Average grain sizes of the different particle size nanodiamond products. *a* 5 nm *b* 50 nm *c* 100 nm *d* 200 nm *e* 250 nm, respectively.



**Figure 6.** TEM and HRTEM images and corresponding SAED patterns (inset) of the different particle size nanodiamond products. *a* 5 nm *b* 50 nm *c* 100 nm *d* 200 nm *e* 250 nm, respectively.

as follows. It is well known that diamond cleavage plane is (111) plane. The man-made diamond is easily separated from the cleavage plane (111) under the effect of external forces. As showed in [scheme 1a](#), synthetic diamond raw material collided with each other which caused separation of the cleavage plane (111) plane under the action of high-speed airflow with a speed of about 1000 m/s. And then, synthetic diamond raw material was further crushed by the mutual extrusion of the stainless

steel balls in the ball mill ([Scheme 1b](#)). The rolled stainless steel balls have uninterrupted strong impact and roll on the artificial diamond, which can cause further separation and crush of the cleavage plane (111) plane. At the same time, the free fall stainless steel balls which reached a certain height collide and crush to the man-made diamond raw material in the ball mill, which accelerated the degree of starting material. Finally, the synthetic diamond raw material was separated into multilayer

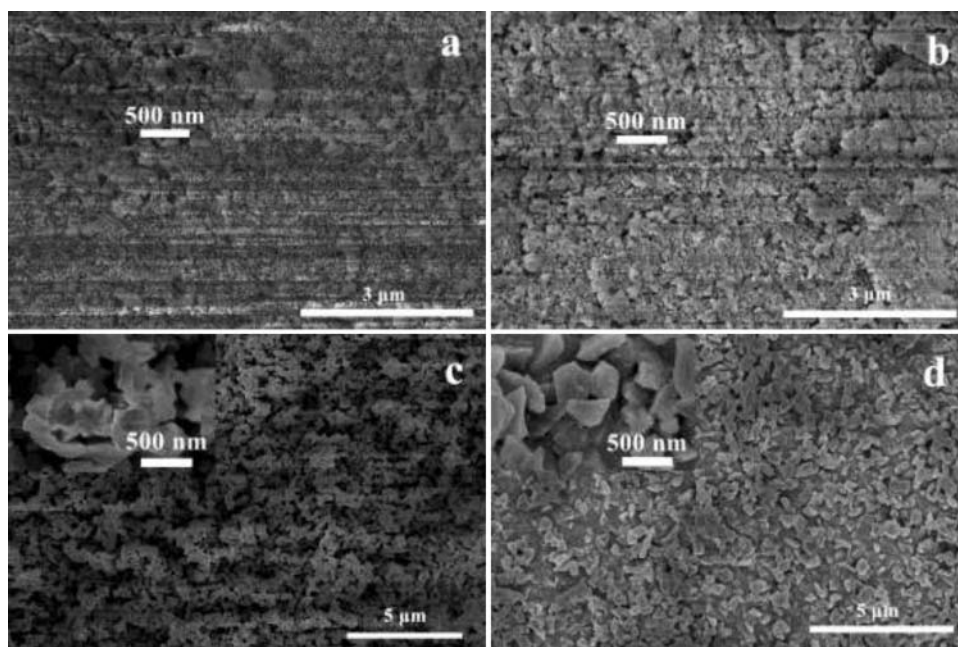


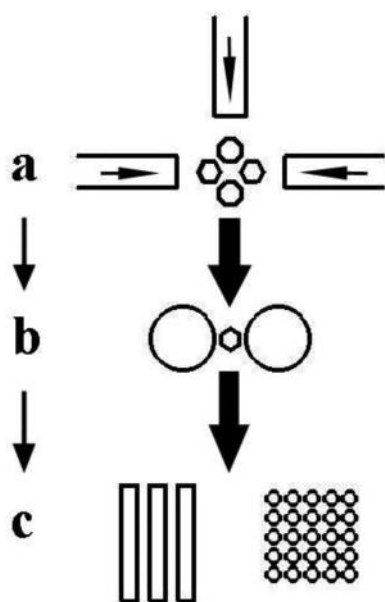
**Figure 7.** SEM images and corresponding high magnification SEM patterns (inset) of the different particle size nanodiamond products. a 50 nm b 100 nm c 200 nm d 250 nm, respectively.

sheets and particles in the cleavage plane (111) under the effect of external forces (Scheme 1c).

The Raman spectra of the as-prepared samples are shown in Figure 8. Obviously, Raman spectra show a smooth curve with the peak at  $\sim 1320\text{ cm}^{-1}$  (D band), the peak at  $\sim 1580\text{ cm}^{-1}$  (G band) and the peak at  $\sim 500\text{ cm}^{-1}$  (amorphous  $\text{sp}^3$  carbon) that are completely absent in sample *a* compared with sample *b-e* in Fig. 8a, which indicating the crystal structure has changed. From Figure 8b to 8e, the Raman spectra show two characteristic features: the D band at  $\sim 1320\text{ cm}^{-1}$ , the G band at  $\sim 1580\text{ cm}^{-1}$ , which correspond to the  $\text{sp}^3$ -bonding carbon (diamond) and  $\text{sp}^2$ -bonding carbon (graphite), respectively.<sup>[36–40]</sup> While D band

is narrow and strong, on the contrary, G band is broad and weak. And more important, the Raman relative intensities and full width at half maximum (FWHM) of the  $\text{sp}^3$ -bonding carbon peak at  $\sim 1320\text{ cm}^{-1}$  (D band) and  $\text{sp}^2$ -bonding carbon peak at  $\sim 1580\text{ cm}^{-1}$  (G band) vary strongly with the increasing particle size, suggesting the crystalline of the samples were increased when the increase of particle size.

Raman spectroscopy is the powerful tool to determine the relative content of the  $\text{sp}^2$  and  $\text{sp}^3$  bonding in the different particle size products. The carbon phase of the different size products can be characterized by measuring the position and width of G-peak and intensity ratio of D- and G-peaks in Raman spectra, rather than by directly measuring their intensities. The fraction of  $\text{sp}^3$  bonding presents in the different particle size products can be evaluated by the peak position of the G peaks. Also, rich information for the confirming the formation of  $\text{sp}^3$  bonds can be obtained from the area and Full Width Half Maxima (FWHM). The  $\text{sp}^3$  contents can be calculated using this



**Scheme 1.** Schematic diagram showing the morphological and structural evolution of the starting material at the different preparation stages.

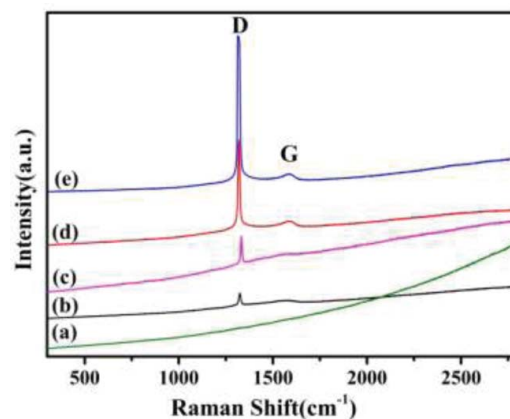


**Figure 8.** Raman spectra of the different particle size nanodiamond products. a 5 nm b 50 nm c 100 nm d 200 nm e 250 nm, respectively.

**Table 2.** Quantities derived from the Raman spectra: FWHM of the D peaks, peak positions  $\omega_D$  and  $\omega_G$  of the D and G peaks,  $sp^3$  content calculated from the G-band position and from the ratios of the area of the D and G-band, respectively.

Particle size/nm	FWHM	$\omega_D$	$\omega_G$	$sp^3$ contents	
				G-position	$A_D/A_G$
50	12.2	1324.3	1593.5	0.174	0.192
100	10.7	1325.9	1592.3	0.18	0.22
200	10	1319.2	1588.3	0.2	0.48
250	9.4	1316	1586	0.21	0.90

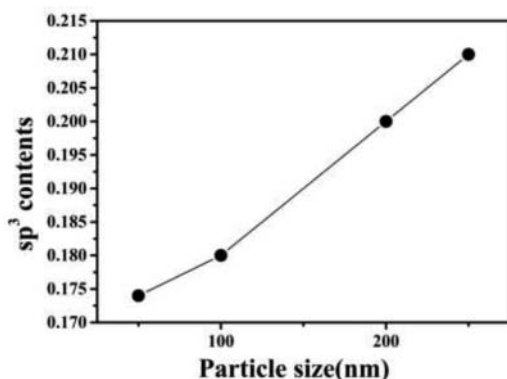


**Figure 9.** Variation of  $sp^3$  contents with different particle size products.

relation as well as from the D- to the G-band area ratio.<sup>[41]</sup> Both methods yield rather similar values when particle size varied between 50 to 100 nm.

$$sp^3 \text{ contents} = 0.24 - 48.9(\omega_G - 0.1580).^{[42]}$$

$$sp^2 \text{ contents} = 1 - sp^3 \text{ contents}$$

In this equation,  $\omega_G$  is the G peak position, which can be taken in the unit of inverse of micrometer unit, as shown in Table 2. However, a reverse trend is observed for both parameters with increased particle size, the FWHM decreases from 12.2 to 9.4 rapidly, whereas, the value of  $\omega_G$  decreases from 1592.3 to 1586  $cm^{-1}$ . The variation of  $sp^3$  contents with particle size shows a linear relation as shown in Figure 9. According to the result, the  $sp^2$  contents increased with increasing particle size, due to layer thickness increased, which is coordinated with the TEM and SEM results.

Micro-Raman analysis of the region shows that the D and G band of sample b (Fig. 8b) exhibits a blue shift of 8  $cm^{-1}$

**Table 3.** Detailed information derived from the solid-state  $^{13}C$  MAS NMR spectra of sample a: peak positions  $\omega_{C1}$  and  $\omega_{C2}$  of the  $C_1$  and  $C_2$  peaks, chemical shift  $\Delta\delta$  between  $C_1$  and  $C_2$  peaks,  $C_2$  content calculated from the ratios of the area of the  $C_1$  and  $C_2$  peaks,  $A_{C2}/A_{C1}$  or  $A_{C2}/(A_{C2}+A_{C1})$ , respectively.

Particle size/nm	$\omega_{C1}$	$\omega_{C2}$	$\Delta\delta$	$C_2$ contents	
				$A_{C2}/A_{C1}$	$A_{C2}/(A_{C2}+A_{C1})$
5	34.6	29.8	4.8	0.5	0.333

compared to sample e (Fig. 8e), due perhaps to the particle size and compressive stress at the  $sp^3:sp^2$  composite layer interface and interlayer.

Comparisons of the different particle size samples produced in the same procedure also showed little difference in structure. Figure 10 shows a typical directly observed, magic angle spinning (MAS), solid state  $^{13}C$  NMR (SSNMR) spectrum of the different particle size products. The experimental spectrum has been fitted to the components, and it is possible to clearly distinguish them all. A resonance centered at  $\delta \sim 34.6$  ppm and additional resonance centered at  $\delta \sim 29.8$  ppm are indicative of parenthetically influenced  $sp^3$  hybridization carbon shown in Fig. 10b.<sup>[43]</sup>  $C_1$  and  $C_2$ , respectively, which suggests that existed two different carbon atoms in sample a product. The prominent feature is the resonance at 34.6 and 29.8 ppm that are broadened by chemical shift distribution and corresponds to variations of carbon atom environments. The chemical shift  $\Delta\delta$  between  $C_1$  peak and  $C_2$  peak is only 4.8 ppm, which indicates two different carbon atoms  $C_1$  and  $C_2$  are similar in the chemical environment. In addition, the  $C_2$  carbon atom contents can be obtained from the ratio of area of  $C_1$  and  $C_2$  peaks,  $A_2/A_1$ . The ratio  $A_2/A_1$  is about 0.5, which indicated that the  $C_2$  carbon atom content is about 33.3%, as shown in Table 3. Moreover, simple calculations show that for ND particles with a diameter less than 5 nm almost 20% of the total numbers of atoms are on the surface.<sup>[18]</sup> With the further decrease of particle size, this value increases drastically, and properties of ND crystals become mainly determined by their surface. Hence, we can conclude that  $C_2$  carbon atom is the surface carbon atom, and exist a carbon atom dimer structure which composed of  $C_1$  and  $C_2$  carbon atom on the surface. The carbon atom dimer perhaps leads to the change of the structure and performance, which is well consistent with the XRD, TEM and Raman results.

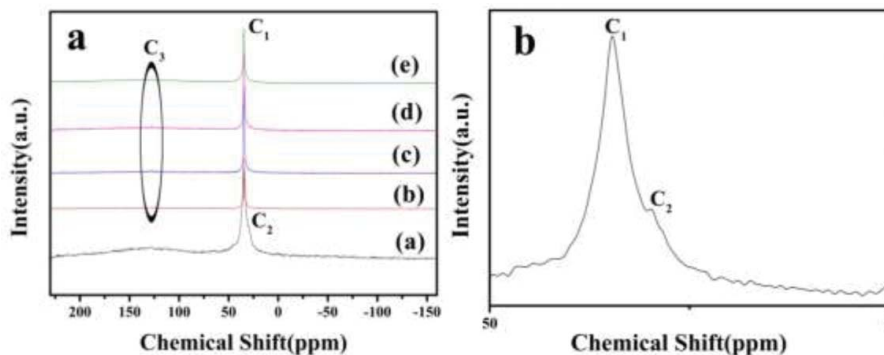


**Figure 10.** (a) Solid-state  $^{13}C$  MAS NMR spectra of the different particle size products, a 5 nm b 50 nm c 100 nm d 200 nm e 250 nm, respectively. (b) Solid-state  $^{13}C$  MAS NMR spectra of the sample a (5 nm) corresponding chemical shift varied between 50 to 0 ppm.

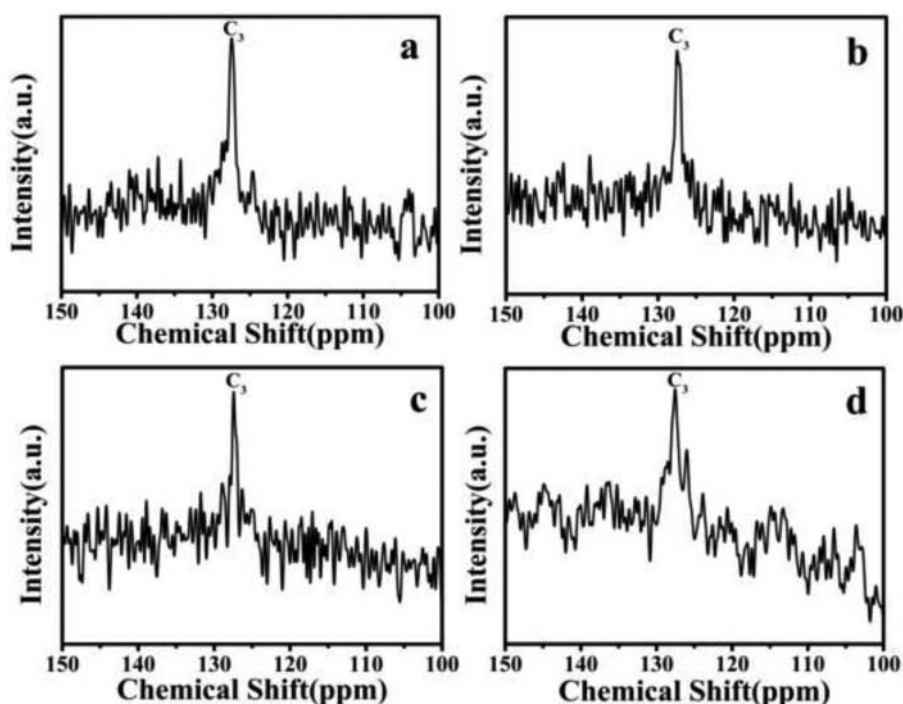


**Figure 11.** Magnification ( $10 \times$ ) of solid-state  $^{13}\text{C}$  MAS NMR spectra of the different particle size products corresponding chemical shift varied between 150 to 100 ppm, *a* 50 nm *b* 100 nm *c* 200 nm *d* 250 nm, respectively.

Figure 10a illustrates comparative solid state  $^{13}\text{C}$  MAS NMR data associated with sample *b-e* products, with Fig. 11 showing the directly observed  $^{13}\text{C}$  MAS NMR spectra at  $\delta \sim 127.8$  ppm ( $\times 10$ ), respectively. The  $^{13}\text{C}$  MAS NMR spectra indicate significant structural change induced by increased particle size. A distinct resonance is observed centered at  $\delta \sim 34.6$  ppm, which corresponds to  $\text{sp}^3$  hybridization carbon, and a weak resonance corresponding to  $\text{sp}^2$  hybridization carbon is also observed at  $\delta \sim 127.4$  ppm.<sup>[44–47]</sup>  $\text{C}_1$  and  $\text{C}_3$ , respectively, while the peak at  $\delta \sim 29.8$  ppm is disappeared. The weak peak centered at  $\sim 34.6$  ppm suggests that existed unsaturated carbon.<sup>[45–47]</sup> which is well consistent with the Raman results.

Previously, we have employed Raman spectroscopy to analyze the  $\text{sp}^2$  contents. In brief, the Raman results clearly indicate the  $\text{sp}^2$  contents increased with the increasing particle size. In addition, detailed information for confirming the formation of  $\text{sp}^2$  hybridization carbon can be obtained from the area and the position of  $\text{C}_1$  and  $\text{C}_3$  peaks. The  $\text{sp}^2$  hybridization carbon contents can be calculated by using the relation as well as from the  $\text{C}_3$  to the  $\text{C}_1$  peak area ratio, as shown in Table 4. However, a

**Table 4.** Information derived from the solid-state  $^{13}\text{C}$  MAS NMR spectra of samples *b-e*: peak positions  $\omega_{\text{C}_1}$  and  $\omega_{\text{C}_3}$  of the  $\text{C}_1$  and  $\text{C}_3$  peaks,  $\text{C}_3$  content calculated from the ratios of the area of the  $\text{C}_1$  and  $\text{C}_3$  peaks,  $A_{\text{C}_3}/A_{\text{C}_1}$  or  $A_{\text{C}_3}/(A_{\text{C}_3}+A_{\text{C}_1})$ , respectively.

Particle size/nm	$\omega_{\text{C}_1}$	$\omega_{\text{C}_3}$	$\text{C}_3$ contents	
			$A_{\text{C}_3}/A_{\text{C}_1}$	$A_{\text{C}_3}/(A_{\text{C}_3}+A_{\text{C}_1})$
50	34.6	127.4	0.031	0.031
100	34.6	127.4	0.036	0.034
200	34.6	127.4	0.047	0.045
250	34.6	127.4	0.053	0.049

forward trend is observed for  $\text{sp}^2$  hybridization carbon contents with increase of particle size, the ratio  $A_{\text{AC}_3}/A_{\text{AC}_1}$  increase from 0.031 to 0.053, suggesting  $\text{sp}^2$  hybridization carbon contents increase from 3.1% to 5.3%, whereas, the value of  $\omega_{\text{AC}_1}$  and  $\omega_{\text{AC}_3}$  are always at  $\delta \sim 34.6$  ppm and 127.4 ppm, respectively. The variation of  $\text{sp}^2$  hybridization carbon contents with particle size shows a linear relation as shown in Figure 12. According to the above result, the  $\text{sp}^2$  hybridization carbon contents increased with increasing particle size, due to the increased layer thickness, which is consistent with the Raman results.

#### 4. Conclusions

Two new pure nanocrystalline diamond of nanoparticles and multilayer nanosheets were prepared through a new cleavage plane crush separation preparation technology by using artificial

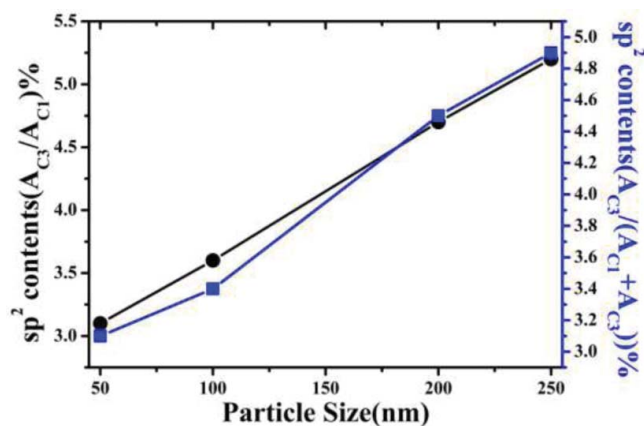


**Figure 12.** Variation of  $\text{sp}^2$  hybridization carbon contents with different particle size products.

diamond as raw material. The precipitation time affected not only the particle size but also the morphologies of the products. Nanoparticles were obtained in the maximum precipitation time of 360 h, and while multilayer nanosheets were obtained for a broader precipitation time range from 168 h to 228 h. Nanoparticles contained carbon atom dimer structure on the surface, while multilayer nanosheets contained unsaturated  $sp^2$  hybridization carbon, and unsaturated  $sp^2$  hybridization carbon contents increased with increasing particle size.

These results demonstrate the use of artificial diamond as starting material for the preparation of nanodiamond is a new and feasible nanodiamond preparation technology, different from the traditional explosive detonation. Moreover, this technique is also capable of improving the morphology and structure of nanodiamond significantly, which opens avenues for numerous new applications of nanodiamond.

## Funding

This work was supported by the Research and Development of Super Hard Materials and Products, Ministry of Science and Technology of the People's Republic of China (Grant No. 2011GH531565).

## References

- Li, Y. L.; Yang, J.; Zhao, Q. H.; Li, Y. Dispersing Carbon-Based Nanomaterials in Aqueous Phase by Graphene Oxides. *Langmuir*. **2013**, *29*, 13527–13534. doi:10.1021/la4024025.
- Bianco, A.; Kostarelos, K.; Prato, M. Applications of carbon nanotubes in drug delivery. *Curr. Opin. Chem. Biol.* **2005**, *9*, 674.
- Sun, X. M.; Liu, Z.; Welsher, K.; Robinson, J. T.; Goodwin, A.; Dai, H. J. Nano-graphene oxide for cellular imaging and drug delivery. *Nano Res.* **2008**, *1*, 203–212. doi:10.1007/s12274-008-8021-8.
- De Jong, W. H.; Borm, P. J. Drug delivery and nanoparticles: applications and hazards. **2009**, *3*, 133.
- Wang, J.; Musameh, M.; Lin, Y. H. Solubilization of carbon nanotubes by Nafion toward the preparation of amperometric biosensors. *J. Am. Chem. Soc.* **2003**, *125*, 2408–2409. doi:10.1021/ja028951v.
- Shao, Y. Y.; Wang, J.; Wu, H.; Liu, J.; Aksay, I. A.; Lin, Y. H. Graphene-based electrochemical sensors and biosensors: a review. *Electroanalysis*. **2010**, *22*, 1027–1036. doi:10.1002/elan.200900571.
- Jariwala, D.; Sangwan, V. K.; Lauhon, L. J.; Marks, T. J.; Hersam, M. C. Carbon nanomaterials for electronics, optoelectronics, photovoltaics, and sensing. *Chem. Soc. Rev.* **2013**, *42*, 2824–2860. doi:10.1039/C2CS35335K.
- Dai, L. M.; Chang, D. W.; Baek, J. B.; Lu, W.; Carbon nanomaterials for advanced energy conversion and storage. *Small*. **2012**, *8*, 1130–1167. doi:10.1002/sml.201101594.
- Kymaksi, E.; Amaratunga, G. Single-wall carbon nanotube/conjugated polymer photovoltaic devices. *Appl. Phys. Lett.* **2002**, *80*, 112–114. doi:10.1063/1.1428416.
- Tung, V. C.; Huang, J. S.; Kim, J.; Smith, A. J.; Chun, C. W.; Huang, J. Towards solution processed all-carbon solar cells: a perspective. *Energy Environ. Sci.* **2012**, *5*, 7810–7818. doi:10.1039/c2ee21587j.
- Ago, H.; Petritsch, K.; Shaffer, M. S. P.; Windle, A. H.; Friend, R. H. Composites of carbon nanotubes and conjugated polymers for photovoltaic devices. *Adv. Mater.* **1999**, *11*, 1281–1285. doi:10.1002/(SICI)1521-4095(199910)11:15%3c1281::AID-ADMA1281%3e3.0.CO;2-6.
- Wang, X. H.; Li, X. J.; Yi, C. H.; Yan, H. H. Water-based gel of nanodiamond powder. *Materials Letters*. **2012**, *73*, 83–85. doi:10.1016/j.matlet.2012.01.011.
- Zhou, D.; Krauss, A. R.; Qin, L. C.; McCauley, T. G.; Gruen, D. M.; et al. Synthesis and electron field emission of nanocrystalline diamond thin films grown from  $N_2/CH_4$  microwave plasmas. *J. Appl. Phys.* **1997**, *82*, 4546–4550. doi:10.1063/1.366190.
- Hiramatsu, M.; Lau, C. H.; Bennett, A.; Foord, J. S. Formation of diamond and nanocrystalline films by microwave plasma CVD. *Thin Solid Films*. **2002**, *407*, 18–25. doi:10.1016/S0040-6090(02)00006-8.
- Makita, H.; Nishimura, K.; Jiang, N.; Ito, T.; Hiraki, A. Ultrahigh particle density seeding with nanocrystal diamond particles. *Thin Solid Films*. **1996**, *281–282*, 279–281. doi:10.1016/0040-6090(96)08652-X.
- Vajpayee, A.; Huhtinen, H.; Awana, V. P. S.; Gupta, A.; Rawat, R.; et al. The effect of nano-diamond additives on the enhancement of critical density and related performance of bulk  $MgB_2$ . *Supercond. Sci. Technol.* **2007**, *20*, S155–S158.
- Ho, D. Beyond the sparkle: the impact of nanodiamond as biolabeling and therapeutic agents. *ACS NANO*. **2009**, *3*, 3825–3829. doi:10.1021/nn9016247.
- Osswald, S.; Yushin, G.; Mochalin, V.; Kucheyev, S. O.; Gogotsi, Y. Control of  $sp^2/sp^3$  carbon ratio and surface chemistry of nanodiamond powder by selective oxidation in air. *J. AM. CHEM. SOC.* **2006**, *128*, 11635–11642. doi:10.1021/ja063303n.
- Roy Greiner, N.; Phillips, D. S.; Johnson, J. D.; Volk, F. Diamonds in detonation soot. *Nature*. **1988**, *333*, 440–442. doi:10.1038/333440a0.
- Volkov, K. V.; Danilenko, V. V.; Elin, V. I. Synthesis of diamond from the carbon in the detonation products of explosives, *Fizika-GoreniiyaiVzryva*. **1990**, *26*, 123–125.
- Mal'kov, I. Y. Containment of carbon in explosion chambers. *Fizika-GoreniiyaiVzryva*. **1993**, *29*, 93–96.
- САВАКИН Г. И.; ТРЕФИЛОВ, ВИ. Формирование структуры и свойства ультрадисперсных алмазов в результате детонации в различных средах конденсированных углеродсодержащих взрывчатых веществ сорциательным кислородным. *ДАН СССР*. **1991**, *321*, 99–103.
- Savvakin, G. I.; Trefilov, V. I. Structure and properties of ultradispersed diamond formed during detonation in various media of condensed, carbon-containing explosives with negative oxygen balance. *Sov. Phys. Dokl.* **1991**, *36*, 785–787.
- Petrov, E. A.; Sakovich, G. V.; Brylyakov, P. M. Conditions for preserving diamonds when produced by explosion. *Sov. Phys. Dokl.* **1990**, *35*, 765–767.
- Kong, H. T.; Wang, L. H.; Zhu, Y.; Huang, Q.; Fan, C. H. Culture medium-associated physicochemical insights on the cytotoxicity of carbon nanomaterials. *Chemical Research in Toxicology*. **2015**, *28*, 290–295. doi:10.1021/tx500477y.
- Zhu, Y.; Li, J.; Li, W. X.; Zhang, Y.; Yang, X. F.; Chen, N.; et al. The biocompatibility of nanodiamonds and their application in drug delivery systems. *Theranostics*. **2012**, *2*, 302–312. doi:10.7150/thno.3627.
- Ozawa, M.; Inaguma, M.; Takahashi, M.; Kataoka, F.; Kruger, A.; et al. Preparation and behavior of brownish, clear nanodiamond colloids. *Adv. Mater.* **2007**, *19*, 1201–1206. doi:10.1002/adma.200601452.
- Mochalin, V. N.; Shenderova, O.; Ho, D.; Gogotsi, Y. The properties and applications of nanodiamonds. *Nat. Nanotechnol.* **2012**, *7*, 11–23. doi:10.1038/nnano.2011.209.
- Gruen, D. M.; Shenderova, O. A.; Vul, A. Y., *Synthesis, Properties and Applications of Ultrananocrystalline Diamond*; The Netherlands: Springer, Dordrecht, **2005**.
- Dolmatov, V. Y. Detonation synthesis ultradispersed diamonds: properties and applications. *Russian Chemical Reviews*. **2001**, *70*, 607–626. doi:10.1070/RC2001v070n07ABEH000665.
- Li, L.; Davidson, J. L.; Lukehart, C. M. Surface functionalization of nanodiamond particles via atom transfer radical polymerization. *Carbon*. **2006**, *44*, 2308–2315. doi:10.1016/j.carbon.2006.02.023.
- Danilenko, V. V. On the history of the discovery of nanodiamond synthesis. *Physics of the Solid State*. **2004**, *46*, 595–599. doi:10.1134/1.1711431.
- Spitsyn, B. V.; Bouilov, L. L.; Derjaguin, B. V. Vapor growth of diamond on diamond and other surfaces. *J. Cryst. Growth*. **1981**, *52*, 219–226. doi:10.1016/0022-0248(81)90197-4.
- Chen, H. C.; Lo, S. C.; Lin, L. J.; Huang, P. C.; Shih, W. C.; et al. The 3D-tomography of the nano-clusters formed by Fe-coating and annealing of diamond films for enhancing their surface electron field emitters. *AIP ADVANCES*. **2012**, *2*, 032153. doi:10.1063/1.4748865.

- [35] Patterson, A. L. The Scherrer Formula for X-Ray particle size determination. *Phys. Rev.* **1939**, *56*, 978. doi:10.1103/PhysRev.56.978.
- [36] Nersisyan, H. H.; Joo, S. H.; Yoo, B. U.; Kim, D. Y.; Lee, T. H.; et al. Combustion-mediated synthesis of hollow carbon nanospheres for high-performance cathode material in lithium-sulfur battery. *Carbon*. **2016**, *103*, 255–262. doi:10.1016/j.carbon.2016.03.022.
- [37] Lou, S. C.; Chen, C. L.; Teng, K. Y.; Tang, C. Y.; Lin, I. N. The synthesis of diamond nano-tips for enhancing the plasma illumination characteristics of the capacitive type plasma devices. *J VacSci Tech B*. **2013**, *31*, 02B19.
- [38] Wei, M.; Yao, K. Y.; Liu, Y. M.; Yang, C.; Zang, X.; Lin, L. W. A solar-blind UV detector based on graphene microcrystalline diamond heterojunctions. *small*. **2017**, *13*, 1701328. doi:10.1002/sml.201701328.
- [39] Yu, J.; Liu, G. X.; Sumant, A. V.; Goyal, V.; Balandin, A. A. Graphene-on-diamond devices with increased current-carrying capacity: carbon  $sp^2$ -on- $sp^3$  technology. *Nano Letters*. **2012**, *12*, 1603–1608. doi:10.1021/nl204545q.
- [40] Yao, K. Y.; Yang, C.; Zang, X.; Feng, F.; Lin, L. W., *Carbon  $sp^2$ - $sp^3$  technology: graphene-on-diamond thin film UV detector, 2014 IEEE 27th International Conference on Micro Electro Mechanical Systems (MEMS)*. San Francisco, CA, **2014**, 1159–1162.
- [41] Ferrari, A. C.; Robertson, J. Interpretation of Raman spectra of disordered and amorphous carbon. *Physical Review B*. **1999**, *61*, 14095–14107. doi:10.1103/PhysRevB.61.14095.
- [42] Praver, S.; Nugent, K. W.; Lifshitz, Y.; Lempert, G. D.; Grossman, E.; et al. Systematic variation of the Raman spectra of DLC films as a function of  $sp^2:sp^3$  composition. *Diamond and Related Materials*. **1996**, *5*, 433–438. doi:10.1016/0925-9635(95)00363-0.
- [43] Cai, W. W.; Piner, R. D.; Stadermann, F. J.; Park, S. J.; Shaibat, M. A.; et al. Synthesis and solid-state NMR structural characterization of  $^{13}\text{C}$ -Labeled graphite oxide. *Science*. **2008**, *321*, 1815–1817. doi:10.1126/science.1162369.
- [44] Thomas, H. R.; Day, S. P.; Woodruff, W. E.; Valles, C.; Young, R. J.; et al. Deoxygenation of Graphene Oxide: Reduction or Cleaning. *Chem. Mater*. **2013**, *25*, 3580–3588.
- [45] Panich, A. M.; Shames, A. I.; Zousman, B.; Levinson, O. Magnetic resonance study of nanodiamonds prepared by laser-assisted technique. *Diamond and Related Materials*. **2012**, *23*, 150–153. doi:10.1016/j.diamond.2011.12.047.
- [46] Panich, A. M.; Shames, A. I.; Sergeev, N. A.; Olszewski, M.; McDonough, J. K.; et al. Nanodiamond graphitization: a magnetic resonance study. *Journal of Physics: Condensed Matter*. **2013**, *25*, 245303.
- [47] Shames, A. I.; Mogilyansky, D.; Panich, A. M.; Sergeev, N. A.; Iaszewski, M. O.; et al. XRD, NMR, and EPR study of polycrystalline micro- and nano-diamonds prepared by a shock wave compression method. *Physica Status Solidi A*. **2015**, *212*, 2400–2409. doi:10.1002/pssa.201532154.